

DEVELOPMENT OF PET FOR TOTAL-BODY IMAGING*

VARSHA VISWANATH^a, MARGARET E. DAUBE-WITHERSPOON^b
JEFFREY P. SCHMALL^b, SULEMAN SURTI^b
MATTHEW E. WERNER^b, GERD MUEHLLEHNER^b
MICHAEL J. GEAGAN^b, AMY E. PERKINS^c, JOEL S. KARP^b

^aUniversity of Pennsylvania, School of Engineering and Applied Sciences
Department of Bioengineering, Philadelphia, USA

^bUniversity of Pennsylvania, School of Medicine, Department of Radiology
Philadelphia, USA

^cPhilips Healthcare, Highland Heights, Cleveland, USA

(Received September 21, 2017)

PET imaging is a key diagnostic tool used clinically to follow and treat disease. While static FDG scans are routine in the clinic, dynamic imaging of disease-specific tracers is important to provide a more precise measure of treatment response. Commercial scanners have limited axial field-of-view and, therefore, we are building a 70 cm long axial FOV TOF PET/CT scanner to enable whole-body dynamic imaging with very high sensitivity. Our scanner is based on detectors with digital SiPMs to provide 300 ps, or better, timing resolution. In this paper, we describe the design and expected performance of this system that will be used for clinical and translational research at the University of Pennsylvania.

DOI:10.5506/APhysPolB.48.1555

1. Introduction

Molecular imaging is increasingly recognized as a precision diagnostic tool [1], since it can be used to survey the entire body and burden of disease in a single imaging session [2]. Molecular imaging's utility in oncology, cardiology, endocrinology, and drug development has been well-demonstrated by ¹⁸F-fluorodeoxyglucose (FDG) and PET/CT, an inherently quantitative imaging modality, while markers such as ¹⁸F-fluoroestradiol (FES) [3, 4] are increasingly being used to determine the likelihood of response based on the

* Presented at the 2nd Jagiellonian Symposium on Fundamental and Applied Subatomic Physics, Kraków, Poland, June 3–11, 2017.

pre-therapy level of tracer uptake. Whole-body PET scans are routinely performed one hour after injection of 10–15 mCi of FDG and are imaged in 8–10 step-and-shoot bed positions, each typically 1.5–3 min in duration, that are knit together to create a quantitatively-accurate static snapshot of glycolytic metabolism in the body. The standardized uptake value (SUV), a semi-quantitative metric that uses patient weight and injected activity to normalize quantitation of uptake across patients and scanners, has become the accepted clinical measure of metabolism. Using SUV, clinicians track the glucose avidity of cancer lesions over time instead of using only structural imaging to track the change in size. An increase in SUV after treatment implies that a patient is unresponsive and that treatment should be altered while decreasing SUV implies a positive response. In some cases, response, as measured by SUV, will be heterogeneous across lesions and can be unaccompanied by structural changes [5]. Therefore, assessment of metabolic processes throughout the body is essential for oncology patients.

While SUV is an effective analog for tracer metabolism in the body, it is merely a snapshot of a dynamic uptake process that reflects a lesion's aggressiveness. An FDG avid lesion that accumulates tracer over minutes is more harmful than a lesion whose SUV drops. In addition to FDG, there are numerous other tracers that characterize various properties of cancers and help elucidate optimal treatments. A few examples of applications and their tracers include hypoxia (^{18}F -FMISO), glutamine pool (^{18}F (2S,4R) 4-fluoroglutamine), bone metastases (^{18}F -fluoride), estrogen receptor expression (^{18}F -FES), diffusion (^{15}O -water), angiogenesis (^{18}F -arginine-glycine-aspartic acid (RGD)), lipid metabolism (^{11}C -choline), oxidative metabolism (^{11}C -acetate), and cellular proliferation (^{18}F -fluorothymidine (FLT)) [6]. Studying both the uptake and dynamic properties of primary and distant metastatic lesions helps guide treatment. Dynamic whole-body imaging is limited in axial coverage with current clinical PET scanners, which have an axial field-of-view (AFOV) of 15–25 cm, chosen as a compromise between scanner cost and axial coverage sufficient to complete a whole-body FDG survey in a reasonable time. However, if a patient has lesions throughout the thorax, abdomen, and pelvis, dynamic scans of all lesions cannot currently be acquired simultaneously. In this case, the primary site is typically chosen to assess response to therapy and one must assume that all areas of disease behave similarly. Therefore, a long AFOV scanner would enable us to capture the kinetics of tracers for larger volumes in the body and to simultaneously study the behavior of multiple organs and interactions between them. To achieve these capabilities, we are building a state-of-the-art, long AFOV TOF PET scanner based on the Philips Vereos digital detectors [7].

2. Recent PET advancements

In the past twenty years, there have been significant advancements in PET instrumentation and imaging methodologies that can be applied to the development of a long AFOV system. Two long AFOV scanners in the 50–70 cm range have been previously built using traditional inorganic scintillators (lutetium oxyorthosilicate (LSO) and bismuth germinate (BGO)); however, these devices have not transitioned to commercial or research use [8, 9]. Additionally, long AFOV scanners designs have been proposed using non-traditional PET detectors such as resistive plate chambers, straw tube drift chambers, and plastic scintillator strips. While these scanners have superb timing and spatial resolution, they trade off detection efficiency for cost [10–12]. Our goal is to take advantage of all recent PET advancements that have been successfully implemented in commercial scanners including fully 3D imaging, quantitative iterative reconstruction, CT attenuation correction, improved scintillators, time-of-flight (TOF), and — most recently — silicon photodetectors. When building our scanner, a scalable design will make it possible to expand the AFOV beyond 70 cm, and build additional scanners with this design with varying AFOVs. A brief history leading up to the current state-of-the-art in PET instrumentation follows, as many of the recent advancements in technology are relevant to our long AFOV scanner design.

Prior to the early 1990s, with a few exceptions such as the 3D imaging NaI PET scanner at UPenn [13], PET scanners were separated into multiple 2D rings by lead septa, and coincidences were only accepted within rings or between neighboring rings. Removing these septa allowed for oblique coincidences and a 5–10× increase in sensitivity, allowing for shorter scan times [14]. Additionally, the implementation of iterative reconstruction algorithms led to improved image quality [15]. In the late 1990s, CT replaced the rotating transmission source for attenuation correction [16, 17]. Although the accuracy of the correction did not greatly improve, the CT scan is acquired in seconds, albeit at a higher dose, and is a valuable anatomic correlate for clinicians when reading PET scans [18]. Clinicians use CT to localize lesions and make decisions about treatment using both lesion size and FDG avidity as biomarkers [5]. Today's most commonly used clinical PET/CT systems include the Siemens mCT, the Philips Ingenuity, and the GE Discovery [19–21]. Within the last five years, scanners have started to move from using photomultiplier tubes (PMTs) to silicon photodetectors (SiPMs). Although it is currently more expensive to utilize SiPMs compared to PMTs, silicon detectors are robust, compact, and can be 1:1 coupled to crystals, negating the need for Anger logic. While the Philips Vereos [7] uses 1:1 coupling with digital SiPMs to achieve a stellar timing resolution (< 320 ps), the newest PET/CT scanner from GE with silicon detectors, the

Discovery MI, still uses light sharing to reduce the total number of SiPMs. In addition, these detectors can be placed inside a magnetic field, so they are optimal for building PET/MR scanners [22–25].

Time-of-flight (TOF) is a key advancement that has improved image quality, patient throughput, and lesion detectability of PET imaging. Good timing resolution is especially valuable when scanning obese patients [26]. Today's clinical PET scanners with conventional PMTs have a timing resolution as good as 500 ps. Historically, BGO was the scintillator crystal of choice for non-TOF imaging, because it is cheap to produce, has a high stopping power, and a high light output. However, due to its poor intrinsic timing properties (decay constant 300 ns), it could not be used for TOF imaging and prompted the move to using cerium-doped LSO/LYSO. These scintillators have a slightly lower stopping power than BGO and are more costly due to their complex manufacturing process. Additionally, background radiation from naturally occurring lutetium (Lu-176; beta decay followed by cascade gamma emissions) may be a contaminant in low dose imaging studies [27]. However, LSO/LYSO has a timing decay constant of 40 ns, which, together with high light output allows for good timing resolution for TOF imaging. An overview of the technology and clinical impact of TOF can be found in [28–30].

3. Advantages of a long axial FOV scanner

While the idea of total-body PET imaging is not new, the push towards building a new system was stimulated by the National Institutes of Health (NIH)-funded Explorer project (Cherry/Badawi, PIs). UC Davis has opted to support the development of a 2 m long PET scanner with SiPM-based detectors and an expected ~ 400 ps timing resolution from United Imaging (China) — which has brought the concept to the forefront of PET research [31–33]. In addition to the ability to perform dynamic whole-body imaging with extended FOV, total-body PET scanners will also be valuable for low-dose/high throughput imaging, whole-body biodistribution/dosimetry studies, and imaging low positron fraction isotopes (*e.g.*, ^{89}Zr). Compared to conventional scanners, longer scanners will have a per organ sensitivity gain of 3–5 due to an increase in solid angle, allowing for ultra-low dose imaging. Thus, research subjects who participate in multiple studies of novel dynamic tracers will have a lower radiation burden from sequential scans. Zhang *et al.* have shown that the increased sensitivity from extending a PET scanner to 2 meters will allow for imaging down to $675 \mu\text{Ci}$ without compromising lesion detectability [34]. Many groups have used simulations to study the sensitivity gain as a function of acceptance angle for various total body PET scanner geometries [35–37] and its effect on lesion detectability [38].

Alternatively, the sensitivity gain can reduce scan time; this could be valuable for pediatric imaging where children undergo general anesthesia (GA) to ensure a lack of motion during the PET study. If total scan time is decreased from ~ 15 min over multiple bed positions to ~ 3 min, then children could forego GA, eliminating associated neurodevelopmental risks [39]. In adult imaging, the decreased scan time with a long AFOV scanner will allow for higher throughput static FDG imaging and better statistics in early frames of dynamic images, which are short (5–10 s) to more accurately determine the peak of the arterial time activity curve (TAC).

We believe the primary advantage of a long AFOV scanner is to image larger volumes of the body and multiple organs simultaneously. This will be valuable when imaging primary cancers with distant metastases, and when conducting biodistribution and dosimetry studies of novel tracers. For current biodistribution studies, 4–5 multi-bed scans are taken over the course of hours, where the subject may require multiple CT scans for attenuation and scatter correction after each break. Today, a 10 mCi injection of FDG is approximately a 7.5 mSv dose for the patient, considerably higher than a low dose CT which can be as low as 1 mSv dose [40]. Because of the increased sensitivity of the long AFOV scanner, there is a potential to use a lower tracer dose for the PET study. Second, since the long AFOV scanner will cover all organs in the thorax and pelvis, multiple bed positions will no longer be required for scanning. Instead, dynamic data can be acquired in a single position. Additionally, a long AFOV scanner will be an ideal means to test the pharmacodynamics of new drugs and filter out ineffective drugs in early stages of testing. Finally, the improved sensitivity and the full body dynamics allows for imaging of theranostic agents, such as monoclonal antibodies (mAb) or chimeric antigen receptor T-cells (CAR-T cells) that are typically tagged with ^{89}Zr [41–43]. After imaging at low dose to confirm tracer distribution, a higher dose will be prescribed as treatment.

4. Scanner design

The first prototype version of the PennPET Explorer scanner will be 70 cm long and cover the majority of the adult torso and pelvis without bed motion, along with whole-body coverage of pediatric patients (Fig. 1). We anticipate the scanner will be operational within a year, and because it is designed to be scalable, where each ring is 23 cm in axial length, it can be extended beyond 70 cm with additional rings, if deemed valuable. It will be coupled to the CT and bed from the Philips Ingenuity scanner [20], and the PET scanner will be based on the Philips Vereos detectors, of which the basic building block is the Philips digital photon counting (PDPC) sensor [44]. The PDPC detector tiles are made of $3.9 \times 3.9 \times 19$ mm³ LYSO

crystals coupled to a digital silicon photomultiplier (dSiPM) developed by Philips. An array of detector tiles (4 transaxial and 7 axial rows) composes one module with a 23 cm AFOV, 18 modules forms one scanner ring, and the full 70 cm scanner is composed of 3 rings. Additionally, each SiPM is one-to-one coupled to individual crystals allowing for a system timing resolution of 320 ps [7] with 10% deadtime from dark noise when cooled to 18°C with a higher timing threshold (trigger 2); in the lab, we have measured timing resolutions of 230 ps at 5°C using lower timing thresholds (trigger 1) with a similar deadtime. We plan to operate the scanner at 5°C with chilled water and by enclosing the electronics in circulating dry air to prevent condensation.

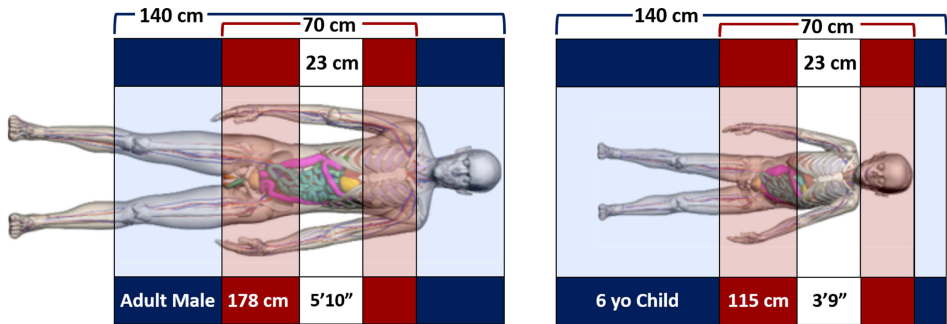


Fig. 1. Schematic showing the region of body spanned by scanners with AFOVs of 23 cm (L23), 70 cm (XL70), and 140 cm (XL140) for (left) an adult male and (right) a 6-year-old child.

In addition to the superb timing resolution at low activity, the timing resolution does not degrade at higher count rates, due to the one-to-one crystal-to-SiPM coupling [7]. This is an important contrast to an Anger-logic PMT-based system where the timing resolution can degrade by 40% at a singles rate of 40 Mcps [45]. The stability of the timing resolution is important for the long AFOV scanner, where high activity organs (*e.g.* heart, bladder, brain) will always fall within the field of view, and the corresponding rings will be operating at higher singles rates. This issue is exacerbated during the first few minutes of a dynamic study, where activity is highly concentrated in the heart as a bolus of tracer passes through the right and left ventricles. If we reach saturation of the data throughput then we can re-organize the data acquisition channels axially, across rings. The axial organization will lower the maximum data rates per processor by a factor of two. Coupled with the sensitivity increase expected from the 70 cm scanner, we expect improved count statistics, accuracy, and temporal resolution in early frames of dynamic studies. Currently, we have successfully built two

full scanner rings (46 cm AFOV), and assembly of the third ring is underway. Once operational, the measured data will be compared with our simulations described in the next section. Images of the scanner components can be seen in Fig. 2.



Fig. 2. Images of one tile (left), module with 28 tiles (middle-left), one ring of the scanner with 18 modules (middle-right), and schematic of the full 2-meter scanner with 9 rings (right).

5. Scanner performance in simulation

Using Geant4 Application for Tomographic Emission (GATE) simulations, we are able to predict sensitivity, image quality, spatial resolution, and count rate performance of the 70 cm PennPET Explorer scanner using NEMA phantoms and simulations of the Vereos scanner as a basis [46, 47]. Timing resolution was set to 320 ps (4.02 ns window) with a 10.9% energy resolution (450–613 keV window) based on the commercial Vereos scanner. Geometric normalizations were created by simulating a 60×70 cm non-attenuating cylinder filled with 1 mCi of activity [48]. Sensitivity was simulated using a 0.25-mCi line source (70 cm long) with one to five attenuating aluminum sleeves (1.25 mm thick), at the center of the scanner. Sensitivity was calculated to be 90.5 kcps/MBq on the 70-cm AFOV scanner and measured to be 5.34 kcps/MBq on the Vereos (16.4 cm AFOV) by Philips [34]. The $18\times$ sensitivity gain agrees with calculations based on geometry and solid angle. Spatial resolution was simulated scanning five 0.1 mCi point sources of ^{18}F for one minute, and reconstructing data using analytic DIRECT [49]; results for the Vereos were reconstructed with 3D-FRP into 1-mm voxels with an axial acceptance angle of $\pm 45^\circ$, and the full width at half maximum (FWHM) was measured according to NEMA standards [47]. Resolution at the center of the 3-ring scanner was 4.06 mm (Vereos: 3.99 mm), while the average transaxial resolution 20 cm off center was 5.31 mm (Vereos: 5.32 mm). Axial resolution at the center of the scanner was 4.49 mm (Vereos: 4.00 mm) and 4.73 mm (Vereos: 4.35 mm) 20 cm radially off center. Contrast recovery coefficients for 10, 13, 17, and

22 mm diameter spheres with a 4:1 contrast in a NEMA IEC phantom, an accepted standard that represents lesions in an FDG patient study, were 0.38, 0.51, 0.59, and 0.68 (Vereos: 0.41, 0.51, 0.63, 0.69) respectively. Simulated data were reconstructed with list-mode TOF-OSEM into 2 mm isotropic voxels [50]. Count rate simulations were performed using a 20.3×70 cm polyethylene cylinder with a 70 cm long line source inserted 4.5 cm below the cylinder's center. The line source was filled with 0.02 to $1.35 \mu\text{Ci}/\text{cc}$ of ^{18}F , and true, scatter, random, and noise equivalent count rates (NECR) were calculated [51]. NECR is related to the square of the signal-to-noise ratio and reflects the expected noise in the reconstructed image. Figure 3 shows that the true rate is linear up to 60 kBq/cc and the NECR has not peaked.

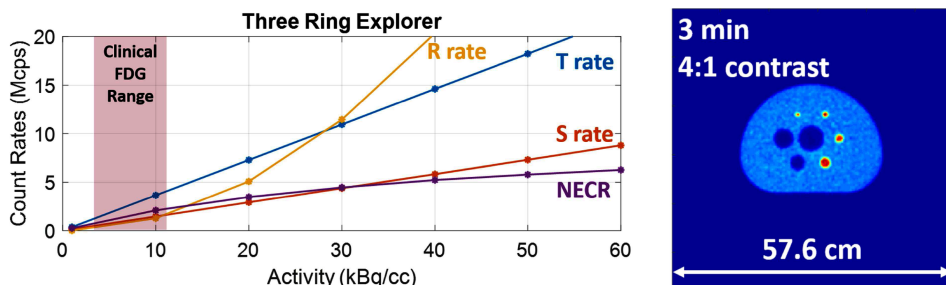


Fig. 3. GATE simulations used to estimate count rate curves for the 3-ring 70-cm scanner (left), including trues (T), scatter (S), randoms (R), and noise equivalent count rates (NECR) are shown, along with a reconstructed image (2-mm thick transaxial slice) of the image quality phantom with 4 hot spheres and 2 cold spheres (right).

Currently, we are studying noise and lesion detectability in the context of low-dose and high-throughput imaging. Using the XCAT phantom [52], we have created a female patient who was injected with 10 mCi of FDG and imaged 1 hour later. We have embedded separately simulated spherical lesions with a 3:1 local contrast [53, 54]. Two lesions were embedded in each lung, four in the liver, and two in the breast, and all lesions are either 7.5 or 10 mm in diameter. Figure 4 shows images of the reconstructed patient. It is important to note that neither cardiac nor respiratory motion was modeled.

Our plan is to use the lesion uptake and precision as metrics to characterize the scanner performance with this 3 minute, 10 mCi dataset. We will also sub-sample the data to study low-dose/high-throughput imaging. Following this static imaging example based on an FDG scan, dynamic patient datasets available at the University of Pennsylvania will be used to model dynamic imaging studies to assess the precision of measured blood input curves, bias and variability of simulated dynamic parameters, and the

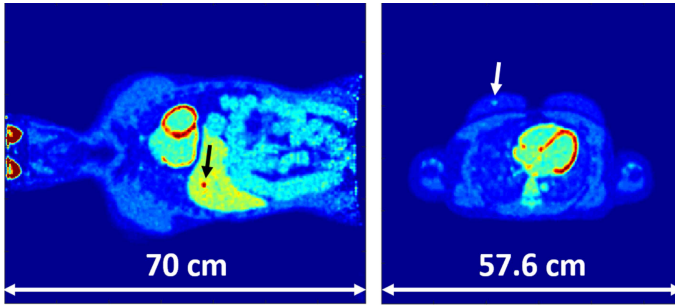


Fig. 4. Axial (left) and transverse (right) images of the female XCAT phantom with lesions in the breast, lung and liver.

effect of improved temporal sampling. Because all dynamic patient datasets are taken over one ~ 20 cm axial bed position, we will use a tracer where patients had lesions at different axial locations in the body. We can then acquire time-activity-curves for each simulated organ from this dataset of patients and use that as an input to our simulations. Lesions will then be embedded, and data will be analyzed using the appropriate compartmental model for the tracer. Most tracers segregate lesions into risk categories, as opposed to simply detecting lesions; therefore, we will use the simulations to better understand the clinical consequences of imaging a patient in the 70-cm scanner. Once the 3-ring scanner is installed in the hospital, we plan corroborate our results with real patient data.

6. Technical challenges

While there are many anticipated benefits to building a total-body PET scanner, there are also many technical challenges to solve. One concern is an axial parallax error from oblique lines of response. To assess this, Schmall *et al.* [31] have looked at the spatial resolution of point sources in various axial locations, and determined that the degradation in resolution is approximately 1 mm when increasing the axial acceptance angle from 12 (18 cm) to 67 (198 cm), where 2 meters is the maximal scanner length under consideration. Although the degradation in the axial spatial resolution is modest, we will include a tilt-dependent resolution model in our reconstruction algorithm to maximize imaging performance.

Another issue is that standard PET corrections (*i.e.* normalization, sensitivity, scatter) are binned into sinograms that grow exponentially in size with AFOV, and both generating these correction files and reconstructing the billions of counts from a study will require efficient methods and parallel computing. Unlike today's commercial scanners, data from the PennPET

Explorer will be read in singles mode and coincidence processing will be done offline. This offers flexibility when determining optimal acceptance angles and handling multiple coincidences; however, it will require TBs of storage. To address these issues, we will implement effective methods to handle the large data sets using commercial off the shelf (COTS) components (computers, data storage, networking) whenever possible, to allow for cost-effectiveness. Finally, it is obvious that the scanner will be costly, so it is important to ensure that the technical gains from extending the scanner's AFOV are reflected in clinical research and patient care. This was the motivation to make the design scalable since the optimal axial length for total-body PET is not yet known.

The PennPET Explorer scanner will be primarily used to study novel tracers; therefore, many studies will exceed an hour where the patient is required to remain still. Thus, it is quite likely that patients will move, so it may be necessary to have a data-driven motion correction option in post-processing. Our group has recently implemented the maximum-likelihood activity and attenuation correction factors (MLACF) reconstruction algorithm based on the histo-image paradigm used in DIRECT [49]. After preliminary testing, this implementation performs comparably to CT based attenuation correction; however, the final outputs still need to be scaled for quantitative accuracy. This could be achieved by placing a marker with a known activity at the edge of the field-of-view to scale the final output. Additionally, the MLACF algorithm will use the CT image for initialization and will account for background radiation from the ^{176}Lu in the crystals, which during low-dose imaging can be non-negligible.

In conclusion, the PennPET Explorer scanner heralds the future of PET imaging. The superb timing resolution, 1:1 crystal-to-SiPM coupling, improved sensitivity, excellent spatial resolution, and linear count-rate performance ensure that the final system will be state-of-the-art, and elucidate questions in the field of nuclear medicine. With the capability for low-dose and total-body imaging, we will study novel tracers in adult patients, and expect that high throughput imaging will negate the risks of putting pediatric patients under general anesthesia. We anticipate performing patient studies on the PennPET Explorer in late 2018.

We acknowledge a Philips research agreement, NIH R01-CA196528 and NIH R01-CA113941. We would also like to acknowledge useful discussions with Andreia Trindade and Pedro Rodrigues at Philips Research in Eindhoven, The Netherlands, along with Chi-Hua Tung at Philips Healthcare in Highland Heights, Ohio. We also gratefully acknowledge contributions from Timothy McDermott.

REFERENCES

- [1] D.A. Mankoff, D.A. Pryma, A.S. Clark, *J. Nucl. Med.* **55**, 525 (2014).
- [2] D.A. Mankoff, M.D. Farwell, A.S. Clark, D.A. Pryma, *JAMA Oncol.* **3**, 695 (2017).
- [3] H.M. Linden *et al.*, *J. Clin. Oncol.* **24**, 2793 (2006).
- [4] M. van Kruchten *et al.*, *Lancet Oncol.* **14**, e465 (2013).
- [5] R.L. Wahl, H. Jacene, Y. Kasamon, M.A. Lodge, *J. Nucl. Med.* **50**, 122S (2009).
- [6] M. Muzi *et al.*, *Magn. Reson. Imaging* **30**, 1203 (2012).
- [7] M. Miller *et al.*, *J. Nucl. Med.* **56**, 434 (2015).
- [8] M. Conti *et al.*, *IEEE Trans. Nucl. Sci.* **53**, 1136 (2006).
- [9] M. Watanabe *et al.*, A High-throughput Whole-body PET Scanner Using Flat Panel PS-PMTs, in: Nuclear Science Symposium Conference Record, 2003 IEEE, 2003, pp. 2442–2446.
- [10] A. Athanasiades *et al.*, Straw Detector for High Rate, High Resolution Neutron Imaging, in: Nuclear Science Symposium Conference Record, 2005 IEEE, 2005, pp. 623–627.
- [11] P. Moskal *et al.*, *Phys. Med. Biol.* **61**, 2025 (2016).
- [12] A. Blanco *et al.*, *Nucl. Instrum. Methods Phys. Res. A* **602**, 780 (2009).
- [13] J.S. Karp *et al.*, *J. Nucl. Med.* **31**, 617 (1990).
- [14] S.R. Cherry, M. Dahlbom, E.J. Hoffman, *J. Comput. Assist. Tomogr.* **15**, 655 (1991).
- [15] C.A. Johnson *et al.*, *IEEE Trans. Nucl. Sci.* **42**, 1223 (1995).
- [16] J.S. Karp, G. Muehllehner, H. Qu, X.-H. Yan, *Phys. Med. Biol.* **40**, 929 (1995).
- [17] M. Daube-Witherspoon, R.E. Carson, M.V. Green, *IEEE Trans. Nucl. Sci.* **35**, 757 (1988).
- [18] P. Kinahan, D. Townsend, T. Beyer, D. Sashin, *Med. Phys.* **25**, 2046 (1998).
- [19] B. Jakoby *et al.*, *Phys. Med. Biol.* **56**, 2375 (2011).
- [20] J.A. Kolthammer *et al.*, *Phys. Med. Biol.* **59**, 3843 (2014).
- [21] M. Teräs *et al.*, *Eur. J. Nucl. Med. Mol. Imaging* **34**, 1683 (2007).
- [22] D.A. Torigian *et al.*, *Radiology* **267**, 26 (2013).
- [23] G. Delso *et al.*, *J. Nucl. Med.* **52**, 1914 (2011).
- [24] C.S. Levin *et al.*, *IEEE Trans. Med. Imaging* **35**, 1907 (2016).
- [25] D.F. Hsu *et al.*, *J. Nucl. Med.* **58**, 1511 (2017).
- [26] J.S. Karp, S. Surti, M.E. Daube-Witherspoon, G. Muehllehner, *J. Nucl. Med.* **49**, 462 (2008).
- [27] M. Conti *et al.*, *Phys. Med. Biol.* **62**, 3700 (2017).
- [28] S. Surti, J.S. Karp, *Physica Medica* **32**, 12 (2016).

- [29] M. Conti, *Physica Medica* **25**, 1 (2009).
- [30] S. Vandenberghe *et al.*, *EJNMMI Phys.* **3**, 3 (2016).
- [31] G. Borasi, F. Fioroni, A. Del Guerra, G. Lucignani, *PET Systems: The Value of Added Length*, Springer, 2010.
- [32] S.R. Cherry *et al.*, *Sci. Transl. Med.* **9**, eaaf6169 (2017).
- [33] J.K. Poon *et al.*, *Phys. Med. Biol.* **57**, 4077 (2012).
- [34] X. Zhang *et al.*, *Phys. Med. Biol.* **62**, 2465 (2017).
- [35] L. Eriksson *et al.*, *Nucl. Instrum. Methods Phys. Res. A* **580**, 836 (2007).
- [36] M. Couceiro, N. Ferreira, P. Fonte, *Nucl. Instrum. Methods Phys. Res. A* **580**, 485 (2007).
- [37] L. Eriksson *et al.*, *IEEE Trans. Nucl. Sci.* **58**, 76 (2011).
- [38] S. Surti, J. Karp, *Phys. Med. Biol.* **60**, 5343 (2015).
- [39] X. Wang, Z. Xu, C.-H. Miao, *PLOS ONE* **9**, e85760 (2014).
- [40] R. Boellaard, *Eur. J. Nucl. Med. Mol. Imaging* **42**, 328 (2015).
- [41] S.A. Grupp *et al.*, *N. Engl. J. Med.* **368**, 1509 (2013).
- [42] M. Kalos *et al.*, *Sci. Transl. Med.* **3**, 95ra73 (2011).
- [43] D.L. Porter *et al.*, *N. Engl. J. Med.* **365**, 725 (2011).
- [44] H. Nöldgen *et al.*, Read-out Electronics for Digital Silicon Photomultiplier Modules, in: 2013 IEEE Nuclear Science Symposium and Medical Imaging Conference (2013 NSS/MIC), Zentralinstitut für Elektronik, 2013.
- [45] S. Surti *et al.*, *J. Nucl. Med.* **48**, 471 (2007).
- [46] D. Strulab *et al.*, *Nucl. Phys. B (Proc. Suppl.)* **125**, 75 (2003).
- [47] N.E.M. Association, N. NU, Standards Publication NU-2-2001: Performance Measurements of Positron Emission Tomography, Rosslyn, VA: National Electrical Manufacturers Association, 2001.
- [48] P.R. Andreia Trindade *et al.*, GATE Simulation of the Philips Vereos Digital Photon Counting PET System NEMA NU2-2012 Characterization, in: IEEE Nuclear Science Symposium and Medical Imaging Conference, San Diego, California, 2015.
- [49] S. Matej *et al.*, *IEEE Trans. Med. Imaging* **28**, 739 (2009).
- [50] L.M. Popescu, S. Matej, R.M. Lewitt, Iterative Image Reconstruction Using Geometrically Ordered Subsets with List-mode Data, in: Nuclear Science Symposium Conference Record, 2004 IEEE, 2004, pp. 3536–3540.
- [51] S. Strother, M. Casey, E. Hoffman, *IEEE Trans. Nucl. Sci.* **37**, 783 (1990).
- [52] W. Segars *et al.*, *Med. Phys.* **37**, 4902 (2010).
- [53] S. Surti *et al.*, *J. Nucl. Med.* **52**, 712 (2011).
- [54] M.E. Daube-Witherspoon, S. Surti, A.E. Perkins, J.S. Karp, *J. Nucl. Med.* **55**, 602 (2014).